Available online at www.sciencedirect.com

jmr&t Journal of Materials Research and Technology

journal homepage: www.elsevier.com/locate/jmrt

Original Article

Strain rate and microtexture analysis of rapid-quenched AA6061 friction stir welds produced with tool eccentricity

Luqman Hakim Ahmad Shah [a,*], *Wentao Hou* [b], *Mohammad Hadi Razmpoosh* [c], *Scott Walbridge* [d], *Adrian Gerlich* [c]

[a] *Faculty of Mechanical and Automotive Engineering Technology, Universiti Malaysia Pahang, 26600 Pekan, Pahang, Malaysia*

[b] *College of Materials Science and Technology, Nanjing University of Aeronautics and Astronautics, Nanjing 211100, China*

[c] *Centre of Advance Materials Joining, Department of Mechanical and Mechatronics Engineering, University of Waterloo, 200 University Avenue West, Waterloo, N2L 3G1 Ontario, Canada*

[d] *Department of Civil and Environmental Engineering, University of Waterloo, 200 University Avenue West, Waterloo, N2L 3G1 Ontario, Canada*

ARTICLE INFO

Article history:
Received 14 August 2022
Accepted 25 September 2022
Available online 29 September 2022

Keywords:
Friction stir welding
Aluminium
Strain rate
Cryogenic
Thermal history
Microtexture
Texture analysis

ABSTRACT

The paper investigates the effect of tool eccentricity on the strain rate and microtextures produced in rapid-quenched AA6061 friction stir welds. Thermocouples are embedded in the tool and the thermal cycle are recorded via a data acquisition system. Stir zone grain refinement is observed in all samples, with the eccentric sample having the finest grains (3.18 μm). The strain rate is measured to be between 0.17 and 51.94 s^{-1}, with the eccentric sample experiencing the highest strain rate. The pole figures indicate crystallographic textures shifted approximately 90° when tool eccentricity is employed. The aligned samples have a strong {11-2}<1-10> B simple shear texture component, while the eccentric sample shows morphological changes towards a strong {11-1}<1-10> A simple shear texture component.

1. Introduction

Friction stir welding (FSW) is a welding process that takes advantage of the rotating motion of a specially designed tool. Heat is generated by friction at the tool–workpiece interface and by severe plastic deformation of the workpiece material, in order to produce an efficient and sound weld. This solid-state joining process avoids many issues arising from the solid–liquid phase transition occurring in conventional fusion welding.

* Corresponding author.
E-mail address: luqmanhakim@ump.edu.my (L.H. Ahmad Shah).

https://doi.org/10.1016/j.jmrt.2022.09.097

Despite the technology being widely used in numerous applications including in additive manufacturing [1–6], some fundamental aspects involving the process response to associated variables including force, torque and strain rate remain a major topic of interest [7–9]. Another topic of concern is the eccentric motion phenomena, i.e., the minute 'wobbling' of the tool or the tool pin during rapid rotation due to the slight offset between the tool's/tool pin's rotational axis and the spindle rotational axis, which can be generated artificially. Numerous works have reported observable metallurgical change when artificial tool eccentricity is imposed into the process [10–14].

Due to the complex material flow during the FSW process, the strain and strain rate remain an intriguing discussion among researchers. This is because characterization of these material parameters is critical, as they directly affect the recrystallization and recovery during the cooling period, which in turn affects the final microstructure [15–17]. Different approaches have been conducted to estimate the strain rate and Table 1 lists some of the notable aluminium alloy-based strain rate measurements in FSW or friction stir related processes (friction stir processing (FSP) and friction stir spot welding (FSSW)), which are reported in the literature.

Efforts have been made to correlate the grain size and temperature measurements within the stir zone during welding to estimate the strain rate during processing based on the relationship between Zener Hollomon parameter (Z) and recrystallized grain size (d) [21,34,35]. Reliable strain rate values can be approximated using the Zener–Hollomon relationship, if the local peak temperature and average grain size can be measured accurately [21]. In this study, the Zener–Hollomon parameter (Z) for aluminium alloys obtained from [36] is used to deduce the strain rate, $\dot{\varepsilon}$ (s^{-1}), of the stir zone through its relationship with the grain size, d (in μm), i.e.:

$$d = [-0.6 + 0.08 \cdot \log(Z)]^{-1} \quad (1)$$

where:

$$Z = \dot{\varepsilon} \cdot \exp\left(\frac{18772}{T_p}\right) \quad (2)$$

and T_p is the peak temperature (in °K) attained during FSW [26].

Since static recrystallization occurs along with dynamic recrystallization once the tool traverses a particular plane, a degree of grain growth can be expected during the cooling cycle and should also be considered [7,15]. Therefore, to obtain more accurate estimates of the strain rate, some experimental works listed in Table 1 employed two methods to retain the as-deformed microstructure without the effects of grain growth, recovery and recrystallization during the cooling period [7,15]. The first one is the 'stop-action' technique [37], i.e. rapidly stopping the tool rotational and translational motion during FSW [15,19,38–40]. In some of these approaches, the tool pin was slightly modified to intentionally break when the translational motion was suddenly accelerated, effectively embedding the pin in the workpiece and preserving the material flow at the periphery of the tool pin [41]. Another equally important method is the subsequent quenching, i.e. rapidly quenching the processed region, usually by cryogenic solutions, in order to suppress further microstructural transformation [39,42].

While the later method is critical in retaining the original as-deformed microstructure, the former is less important if the region of interest is immediately at the wake of the workpiece-tool shoulder interface, where little to no additional deformation imposed by the tool is taking place. This study therefore aims to observe the microstructural evolution and strain rate of AA6061 alloy through cryogenic rapid quenching. The influence of tool eccentricity on strain rate is also evaluated for the first time here using the cryogenic quenching method to preserve microstructures with better fidelity.

Table 1 – Strain rate measurements in aluminium alloy FSW or friction stir related processes.

No.	Authors	Process	Al alloy	Thickness	Max strain rate, $\dot{\varepsilon}$ (s^{-1})	Measurement approach
1	Morisada et al. [18]	FSW	AA1050	5 mm	13.4	X-ray radiography
2	Liu et al. [19]	FSW	AA2024	3 mm	650	Stop action
3	Gerlich et al. [20]	FSSP	AA2024	6.3 mm	1600	Rapid quenching
4	Gerlich et al. [21]	FSSP	AA5754, AA6061	5 mm, 6.3 mm	497, 395	Rapid quenching
5	Gerlich et al. [22]	FSSP	AA7075	1.5 mm	650	Rapid quenching
6	Chen and Cui [23]	FSP	A356	8 mm	85	Pin break
7	Long et al. [24]	FSP	AA5083, AA7050, AA2219	9.5 mm, 9.5 mm, 8.3 mm	350	Simulation
8	Jata & Semiatin [25]	FSW	Al–Li–Cu alloy	7.6 mm	10 (at TMAZ[a])	Experimental
9	Frigaard et al. [26]	FSW	AA6082, AA7108	6 mm	20	Simulation
10	Mukherjee & Ghosh [27]	FSW	AA5083	8 mm	87	Simulation
11	Masaki et al. [28]	FSP	AA1050	10 mm	2.7	Experimental Simulation
12	Arora et al. [29]	FSW	AA2524	6.4 mm	9	Simulation
13	Khan et al. [30]	FSW	AA2219, AA7475	2.5 mm	6.95	Experimental
14	Buffa et al. [31]	FSW	AA7075	3 mm	8	Simulation
15	Nandan et al. [32]	FSW	AA6061	12.7 mm	100	Simulation
16	Zhang & Wu [33]	FSW	AA6061	Not available	22	Simulation

[a] TMAZ: thermo-mechanically affected zone.

2. Materials and method

2.1. Base material and tool design

In this study, bead-on-plate welding was performed on 9.5 mm thick plates of heat-treatable AA6061-T6511 aluminium alloy, with nominal chemical compositions. All specimens were cut to 15 × 7 × 9.5 mm dimensions and were welded with a tool made from H13 tool-steel, with a 9.3 mm pin length as well as 15 mm of shoulder diameter and 6 mm pin diameter measured at the pin base. The tool profile consists of an 8° tapered, M6 threaded with three flats. The tool rotation is counter-clockwise direction as viewed from the top. The weld travel direction was parallel to the rolling direction (RD) using welding parameters summarized in Table 2.

As shown in Table 2, a typical FSW tool setup was used to maintain the tool in the concentrically aligned state. However, another tool spindle holder was designed to provide a 0.4 mm eccentric motion during the tool rapid rotation, as explained elsewhere [43]. The designations for the three specimens observed are tabulated in Table 3.

2.2. Peak temperature and strain rate measurements

Due to limitations in the tool setup, the peak temperature was measured in a second set of repeated experiments with identical welding parameters. To measure the peak temperature at the top region of the stir zone, through-holes were drilled at the tool shoulder and K-type thermocouples were fixed using Omegabond "600" High Temperature Chemical Set Cement such that the end of the thermocouple junction is flush with the shoulder surface. The schematic of the thermocouple setup can be found in [8]. The thermocouple probe therefore remained in contact with the workpiece during the whole welding period. The temperature measurements during FSW process were recorded using a Data Logger MSR145, which was fixed securely on the rotating spindle through a fabricated fixture. The sampling rate was 1 Hz and all conditions were repeated three times to ensure repeatability. The thermocouples embedded in the tool were calibrated against a reference thermocouple and the recorded values re-adjusted after finishing all the weld settings to ensure accurate reading.

To inhibit grain growth and morphological changes associated with the cooling period, a cryogenic rapid quenching process was devised using a mixture of ethylene glycol and purified water to provide a sub-zero freezing temperature. This solution can reach a minimum freezing point approximately −50 °C with 55% water mixture [44]. Liquid nitrogen was incrementally poured into the ethylene glycol + H_2O liquid mixture until a cryogenic temperature of approximately −40 °C was achieved, where the mixture begins to solidify. Then, as it begins to melt, the mixture was used to quench the welds. The mixture was then poured on the workpiece immediately after the tool traverse motion was stopped and pulled out from the workpiece. This method can provide a more rapid quench compared to using liquid nitrogen as nitrogen forms a thin vapor layer once in contact with the workpiece, which insulates it and lowers the cooling rate.

Table 2 – FSW parameters to produce bead-on-plate specimens.

Welding parameter	Value
Tool tilt angle	2.5°
Plunge rate	16 mm/min
Dwell time	10 s
Weld speed	63 mm/min
Rotational speed	710 rpm, 1120 rpm
Tool eccentric setup	Aligned, 0.4 mm eccentricity

Table 3 – Designation of specimens for strain rate analysis.

Tool setup	Rotational speed (rpm)	
	710	1120
Aligned	A-710	A-1120
0.4 mm eccentricity	–	E-1120

To observe in detail the microstructural and texture evolution, samples for high-resolution electron backscatter diffraction (EBSD) analysis were extracted from the top plane of the stir zone (SZ), immediately behind the final shoulder boundary, as shown in the area of interest in Fig. 1(a). This area was selected based on several reasons. Firstly, Suhuddin et al. [45] have reported that the extruded material behind the pin undergoes additional deformation induced by the shoulder. Hence, analysing the area just outside this region may provide more insight in to the severity of deformation, since not additional deformation at the SZ is expected. The thermally activated grain morphology during cooling period can be inhibited through more rapid quenching at the surface using the cryogenic mixture. It is also possible to monitor the top surface temperature using a contact-based thermometer to ensure cryogenic conditions are maintained throughout the cooling period.

15 mm × 7 mm × 9.5 mm specimens were prepared by standard sample preparations. SiC abrasive pads up to 2400 grit were utilized to remove surface asperities (weld bands), followed by the standard aluminium alloy polishing procedures. The surface removal was carefully performed to ensure that the examined area is kept as close to the top surface where maximum quenching occurred. Since the sample surface was mainly prepared manually, slight variations in the amount of top surface removal are expected. Measurements using a micrometer indicate the variance to be in the range of 50–150 μm, as approximated by the thickness of the red line in Fig. 1(b). However, it can be safely assumed that such minor discrepancies do not affect the cooling rate and morphology of the specimens.

The EBSD analysis was performed using a JEOL JSM-7000F equipped with a Schottky field emission gun and a Nordlys II EBSD Camera with HKL Channel analysis software to process inverse pole figure maps. The EBSD characterization was performed with a 1 μm step size on a 150 × 150 μm grid. The observed area was slightly to the retreating side of the weld centre, where the microstructure is expected to be more mechanically stable (Fig. 1(b)). Based on the proposed Nunes kinematic model [46,47], an unstable conglomeration of two distinct material flows originating from retreating side

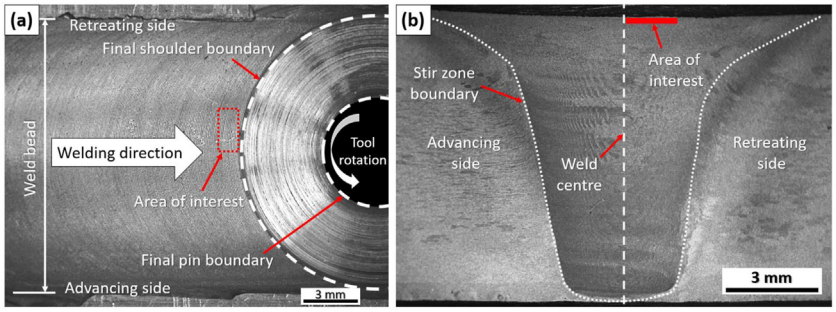

Fig. 1 – Extracted area of interest for EBSD analysis as viewed from (a) top plane and (b) cross-sectional plane at the area of interest in (a).

(straight through current) and advancing side (whirlpool current) may exist in the weld centre, which can potentially yield inconsistencies in the results.

3. Results and discussion

3.1. *Peak temperature*

The thermal cycles of the A-710 and A-1120 sample are shown in Fig. 2. The vertical dashed lines delineate the various periods associated with FSW, namely the tool plunge period, the tool dwelling period, followed by the tool translational traverse period, and finally tool pull-out, which initiates the cooling period. Relatively similar heating rates were observed for both samples. However, the average peak temperature of the traverse period measured in the A-1120 specimen is higher (566 °C) compared to the A-710 specimen (525 °C), stabilizing just below the solidus temperature of the alloy, T_m = 582 °C [48].

Fig. 3 depicts the average peak temperature during the traverse period of the aligned samples as a function of rotational speed. To better understand the peak temperature-rotational speed correlation, two other rotational speeds, i.e., 900 rpm and 1400 rpm, were also measured. The peak temperature increases with rotational speed, with the highest measured temperature at approximately the solidus temperature of AA6061.

While reasonable measurements were obtained for the aligned samples, inconsistencies of the measured peak temperature were recorded for the 0.4 mm eccentric setup, likely due to the rigorous vibration on the system induced by the tool eccentric motion, resulting in unstable thermocouple measurements. The peak temperature values for the eccentric setup, which were well above the solidus temperature (ranging between 600 °C and 626 °C), were thus deemed unreliable. It is speculated that the addition of eccentricity may cause an increase in heating rate and possibly higher peak temperature. However, the peak temperature for A-1120 has shown to stabilize just below the solidus temperature, which is already close to the maximum value. Based on the self-regulated 'slip-stick' mechanism proposed by Schneider et al. [49], once the solidus temperature is reached, local melting occurs at the tool–workpiece interface, changing the contact mechanism from stick to slip, which would regulate the temperature to not exceed the solidus temperature of the workpiece. Therefore, it can be estimated that the 0.4 mm eccentric setup with 1120 rpm rotational speed will produce a similar peak temperature to the aligned tool setup.

3.2. *Strain rate and microstructural texture*

Fig. 4 shows the top surface EBSD inverse pole figure (IPF) maps for all three samples. The high angle boundaries (HAGBs, >°15) are shown as black lines, while the white dashed lines represent the boundary between bands of grains

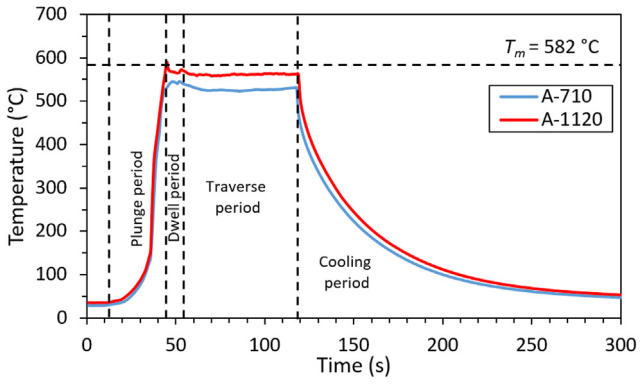

Fig. 2 – Thermal cycle of specimens produced with the aligned tooling.

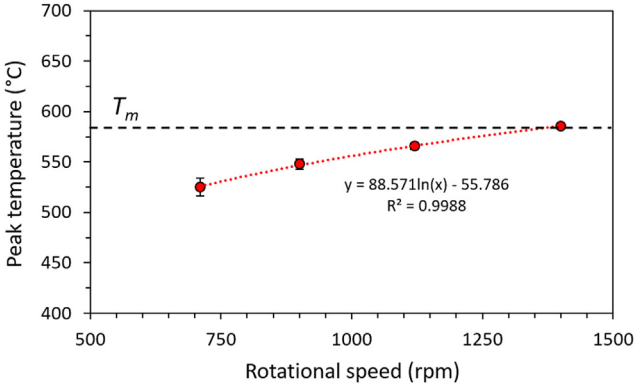

Fig. 3 – Average peak temperature during traverse period of aligned samples as a function of rotational speed.

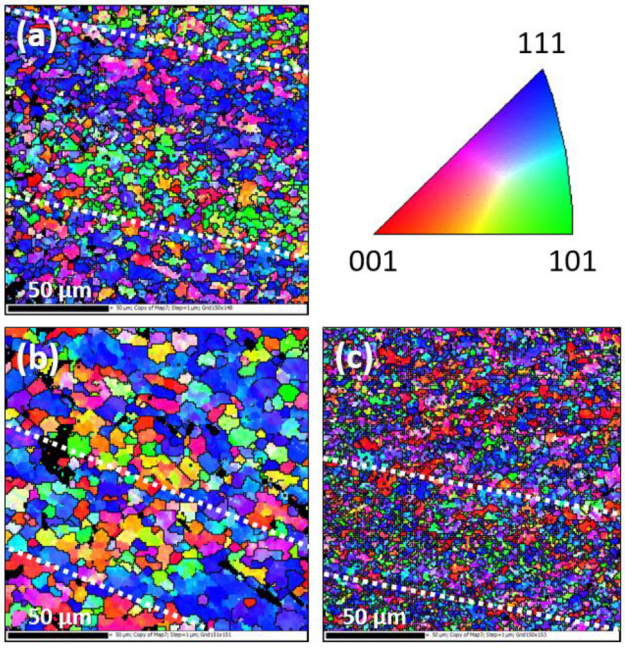

Fig. 4 – IPF maps of (a) A-710, (b) A-1120 and (c) E-1120. The HAGBs are represented by the black lines. Welding direction is upwards.

that formed in layers, which were spaced at a distance equal to the advance per revolution (welding speed/rotational speed), i.e., 0.089 mm/rev for A-710 and 0.056 mm/rev for both A-1120 and E-1120, respectively. The welding direction is upwards. The white lines are inclined at an angle since the observed area is slightly deviated from the SZ centre and towards the retreating side of the SZ (Fig. 1(b)).

In general, the IPF maps show the formation of equiaxed grains on the top surface of the SZ. Furthermore, with similar tool setup, the A-710 specimen shows finer grains compared to the A-1120 sample. However, the weld made with the eccentric tool, i.e., E-1120, has a much finer grains as compared to A-1120 and A-710. This seems to indicate that eccentricity significantly enhances shearing activity in the SZ, refining the grains.

The grain size, peak temperature and calculated strain rate of the samples are shown in Table 4. The grain sizes (d) of the HAGBs were measured using the ASTM E112-13 linear intercept method [50]. The strain rates were then calculated using Equations (1) and (2). The calculated strain rates show values with differences in one or two orders of magnitude between each other. The strain rate range is between 0.17 and 51.94 s^{-1}, where the A-1120 sample show the lowest strain rate. In contrast, the value increased significantly by two orders of magnitude for the E-1120 sample. This further supports the hypothesis that shear stress dominates using the eccentric tool.

Previous works have reported that higher rotational speeds strongly correlate to higher strain and strain rates [21,24,51]. The maximum strain rates reported in the literature to date has been summarized by Kumar et al. [51]. In general, the maximum strain rate exhibits an increasing trend with increasing tool rotational speed. However, the calculated strain rates in this study seem to show a decreasing trend with higher rotational speed. The reduced strain rate calculated for the A-1120 specimen compared to that of the A-710 specimen made with a reduced rotation speed is counter-intuitive. Given the welding temperature was close to the solidus temperature of the base material for the A-1120 sample, this likely indicates that either the actual strains are lower due to local surface melting and tool slippage, or that there was still lingering grain growth on cooling [21].

In comparison, Gerlich et al. [21] conducted FSSW strain rate measurements on similar AA6061 alloy and obtained a maximum peak temperature of 541 °C and strain rate values in the range of 55–395 s^{-1}. The difference in the strain rate range is possibly due to the difference in the method (spot welds versus linear welds), the rotational speed (3000 rpm versus 1120 rpm) as well as the finer grain sizes observed in the base material since it had a reduced thickness (6.3 mm versus 9.5 mm). The highest peak temperature in our work (566 °C) is slightly higher, but remains below the solidus temperature of the alloy (582 °C).

In addition, grain size correlates to the slip-stick condition mentioned earlier. It is possible that the lower rotation rate corresponds to a stick condition that eases as the rotation rate (and temperature) increase, leading to more retained deformation at the lower rotation rate and more recovery/recrystallization at the higher rotation rate. Another possible reason for the discrepancy of the current study to other previous works may be due to the correlative effect of strain rate and temperature. Based on friction stir processing of dual phase TWIP steel Razmpoosh et al. [35] has suggested that decreasing grain size is formed in the SZ at relatively lower rotational speed (800–1600 rpm), which minimizes at 1600 rpm as the strain rate balances with the temperature. After this minimum grain size parameter, the temperature effect overcomes the strain rate and grain size constantly increases with increasing rotational speed. It is therefore plausible that, for AA6061 alloys, the strain rate-temperature balance and minimum grain size threshold has been reached in close proximity to the A-710 sample rotational speed, followed by an increasing grain size trend with further increase in rotational speed (A-1120), where the temperature effect overcomes the strain rate.

Fig. 5 shows the IPFs of all samples based on the area observed in Fig. 4. The IPFs are shown in the normal direction

Table 4 – Grain size, peak temperature and calculated strain rate of samples.

Tool setup	Rotational speed (rpm)	EBSD grain size, w (μm)	Peak temperature, T_p (Kelvin)	Calculated strain rate, $\dot{\varepsilon}$ (s^{-1})
Aligned	710	4.24 ± 0.68	798.15	1.71
	1120	8.63 ± 0.88	839.15	0.17
Eccentric	1120	3.18 ± 1.54	839.15	51.94

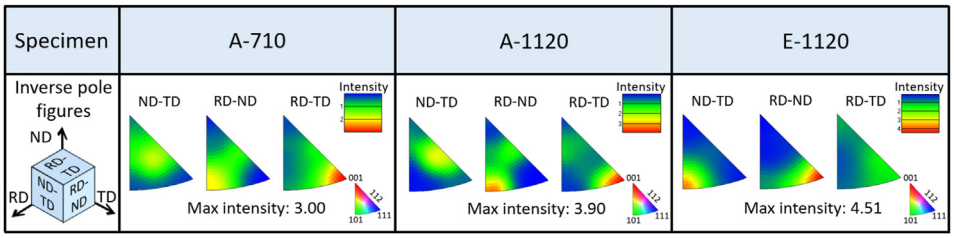

Fig. 5 – IPFs of all samples based on the observed area in Fig. 4.

(ND), rolling direction (RD), which coincides with the welding direction, and transverse direction (TD). Likewise, the plane of reference is indicated by RD-TD plane (top plane), ND-TD plane (front plane, perpendicular to the rolling direction) and RD-ND plane (side plane, parallel to the rolling direction).

Differences between the aligned and eccentric samples can be observed in the IPFs. For aligned tool samples, the {111} plane and <011> direction are roughly parallel to the top plane, which corresponds to the directions with the maximum shear stresses induced by the tool shoulder [52]. As a result of this dominant orientation of the shear deformation, the IPFs of the A-710 and A-1120 samples show a maximum intensity of the {111} plane towards the ND (RD-TD plane), in conjunction with high intensity of the {011} plane being plane normal to the TD (RD-ND plane). Previous works have also reported similar observations with regards to the workpiece–pin interface, where the {111} plane and <011> direction are preferentially oriented parallel to the tool pin/shoulder interface, i.e. location of maximum shear stresses [47,52–54].

However, the IPFs of the E-1120 sample show an approximately 90° shift of the {111} and {011} plane towards the TD (RD-ND plane) and the RD (ND-TD plane), respectively. It is postulated that the observed change in the texture orientation corresponds to a change in the ideal shear texture, indicating a variation in shear deformation strength as a result of the tool eccentric motion.

In addition, based on works by Fonda and Bingert [55], further analysis of the texture data indicated that both A-710 sample and A-1120 samples have a strong {11-2}<1-10> B simple shear texture component. In contrast, with the eccentric setup, the E-1120 sample shows morphological changes towards a strong {11-1}<1-10> A simple shear texture component.

Since the observed area is limited and FSW textures vary as a function of position relative to the tool [54,56], future work encompassing larger areas and larger sampling sizes through iterations and parameter optimization is suggested to further elucidate the discrepancy observed [57–61].

4. Conclusion

A rapid-quenched technique was successfully utilized on AA6061 friction stir welds to examine the change in strain rate and microtexture. The important findings of the research presented in this paper are as follows:

(1) Peak temperature increases with increasing rotational speed, but remains below the solidus temperature during the translational motion of the tool in the case of bead-on-plate welding of AA6061 with and without tool eccentricity.
(2) Grain refinement of the stir zone is observed for all welding conditions, with the 0.4 mm eccentricity setup having the finest average grain size of 3.18 μm.
(3) The calculated strain rate is between 0.17 and 51.94 s^{-1}, where the E-1120 sample shows a significant increase of two orders of magnitude compared to its A-1120 counterpart.
(4) The IPFs of the E-1120 sample show an approximately 90° shift of the {111} and {110} plane from the generally preferred RD-TD plane and ND-RD plane orientation towards the ND-RD plane and ND-TD plane orientation, respectively.
(5) The aligned samples have a strong {11-2}<1-10> B simple shear texture component, while the eccentric sample shows morphological changes towards a strong {11-1}<1-10> A simple shear texture component.

Author contributions

Luqman Hakim Ahmad Shah: Investigation, Formal analysis, Data curation, Visualization, Writing-original draft.

Wentao Hou: Investigation, Formal analysis.

Mohammad Hadi Razmpoosh: Investigation, Formal analysis, Visualization.

Scott Walbridge: Supervision, Funding acquisition.

Adrian Gerlich: Supervision, Conceptualization, Writing-review & editing, Funding acquisition.

Declaration of Competing Interest

The authors declare that they have no known competing financial interests or personal relationships that could have appeared to influence the work reported in this paper.

Acknowledgements

This work was supported by the Natural Sciences and Engineering Research Council of Canada (NSERC); Ministry of

Higher Education, Malaysia; and research grant from University Malaysia Pahang, Pahang, Malaysia (PDU203208). EBSD microscopy was performed at the Canadian Centre for Electron Microscopy at McMaster University, which is supported by NSERC and the Canadian Foundation for Innovation.

REFERENCES

[1] Lohwasser D, Chen Z. Friction stir welding: from basics to applications. Cambridge, England: Woodhead Publishing Limited; 2010.
[2] Mishra RS, Mahoney MW. Friction stir welding and processing. 1st ed. Materials Park, Ohio: ASM International; 2007.
[3] Gibson BT, Lammlein DH, Prater TJ, Longhurst WR, Cox CD, Ballun MC, et al. Friction stir welding: process, automation, and control. J Manuf Process 2014;16:56–73. https://doi.org/10.1016/j.jmapro.2013.04.002.
[4] Mishra RS, Haridas RS, Agrawal P. Friction stir-based additive manufacturing. Sci Technol Weld Join 2022;27:141–65. https://doi.org/10.1080/13621718.2022.2027663.
[5] Srivastava M, Rathee S, Maheshwari S, Noor Siddiquee A, Kundra TK. A review on recent progress in solid state friction based metal additive manufacturing: friction stir additive techniques. Crit Rev Solid State Mater Sci 2019;44:345–77. https://doi.org/10.1080/10408436.2018.1490250.
[6] Chaudhary B, Kumar N, Murugesan J. Exploring temperature-controlled friction stir powder additive manufacturing process for multi- layer deposition of aluminum alloys. J Mater Res Technol 2022;20:260–8. https://doi.org/10.1016/j.jmrt.2022.07.049.
[7] Mishra RS, De PS, Kumar N. Friction stir welding and processing: science and engineering. Switzerland: Springer International Publishing; 2014. https://doi.org/10.1007/978-3-319-07043-8.
[8] Shah LH, Fleury A, St-George L, Walbridge S, Gerlich AP. Evolution of process parameters in friction stir welding of AA6061 aluminum alloy by varying tool eccentricity. Int J Adv Manuf Technol 2020;109:1601–12.
[9] Han S, Masood U, Yoon J, Jun T. Investigating local strain rate sensitivity of the individual weld zone in the friction stir welded DP. J Mater Res Technol 2022;20:508–15. https://doi.org/10.1016/j.jmrt.2022.07.125.
[10] Hou W, Ding Y, Huang G, Huda N, Shah LHA, Piao Z, et al. The role of pin eccentricity in friction stir welding of Al-Mg-Si alloy sheets: microstructural evolution and mechanical properties. Int J Adv Manuf Technol 2022;121:7661–75. https://doi.org/10.1007/s00170-022-09793-x.
[11] Shah LH, Walbridge S, Gerlich A. Tool eccentricity in friction stir welding: a comprehensive review. Sci Technol Weld Join 2019;24:566–78. https://doi.org/10.1080/13621718.2019.1573010.
[12] Ahmad Shah LH, Midawi ARH, Walbridge S, Gerlich A. Influence of tool eccentricity on the material flow and microstructural properties of AA6061 aluminum alloy friction stir welds. J Alloys Compd 2020:826. https://doi.org/10.1016/j.jallcom.2020.154219.
[13] Shah LH, Huda N, Esmaeili S, Walbridge S, Gerlich AP. Structural morphology of Al-Mg-Si alloy friction stir welds through tool eccentricity. Mater Lett 2020;275:128098. https://doi.org/10.1016/j.matlet.2020.128098.
[14] Chen Y, Wang H, Wang X, Ding H, Zhao J, Zhang F, et al. Influence of tool pin eccentricity on microstructural evolution and mechanical properties of friction stir processed Al-5052 alloy. Mater Sci Eng, A 2019;739:272–6. https://doi.org/10.1016/j.msea.2018.10.057.
[15] Prangnell PB, Heason CP. Grain structure formation during friction stir welding observed by the "stop action technique. Acta Mater 2005;53:3179–92. https://doi.org/10.1016/j.actamat.2005.03.044.
[16] Ma ZY, Feng AH, Chen DL, Shen J. Recent advances in friction stir welding/processing of aluminum alloys: microstructural evolution and mechanical properties. Crit Rev Solid State Mater Sci 2018;43:269–333. https://doi.org/10.1080/10408436.2017.1358145.
[17] Jiang W, Jiang X, Yuan T, Chen S, Liu Y, Liu X. Material flow and viscous slips during stationary shoulder friction stir welding of Ti6Al4V. Sci Technol Weld Join 2022;27:220–7. https://doi.org/10.1080/13621718.2022.2036573.
[18] Morisada Y, Imaizumi T, Fujii H. Determination of strain rate in friction stir welding by three-dimensional visualization of material flow using X-ray radiography. Scripta Mater 2015;106:57–60. https://doi.org/10.1016/j.scriptamat.2015.05.006.
[19] Liu X, Wu C, Padhy GK. Characterization of plastic deformation and material flow in ultrasonic vibration enhanced friction stir welding. Scripta Mater 2015;102:95–8. https://doi.org/10.1016/j.scriptamat.2015.02.022.
[20] Gerlich A, Su P, Yamamoto M, North TH. Effect of welding parameters on the strain rate and microstructure of friction stir spot welded 2024 aluminum alloy. J Mater Sci 2007;42:5589–601. https://doi.org/10.1007/s10853-006-1103-7.
[21] Gerlich A, Yamamoto M, North TH. Strain rates and grain growth in Al 5754 and Al 6061 friction stir spot welds. Metall Mater Trans A 2007;38:1291–302. https://doi.org/10.1007/s11661-007-9155-0.
[22] Gerlich A, Avramovic-Cingara G, North TH. Stir zone microstructure and strain rate during Al 7075-T6 friction stir spot welding. Metall Mater Trans A Phys Metall Mater Sci 2006;37:2773–86. https://doi.org/10.1007/BF02586110.
[23] Chen ZW, Cui S. Strain and strain rate during friction stir welding/processing of Al-7Si-0.3Mg alloy. IOP Conf Ser Mater Sci Eng 2009;4:012026. https://doi.org/10.1088/1757-899X/4/1/012026.
[24] Long T, Tang W, Reynolds AP. Process response parameter relationships in aluminium alloy friction stir welds. Sci Technol Weld Join 2007;12:311–7. https://doi.org/10.1179/174329307X197566.
[25] Jata KV, Semiatin SL. Continuous dynamic recrystallization during friction stir welding of high strength aluminum alloys. Scripta Mater 2000;43:743–9.
[26] Ø Frigaard, Grong Ø, Midling OT. A process model for friction stir welding of age hardening aluminum alloys. Metall Mater Trans A 2001;32:1189–200. https://doi.org/10.1007/s11661-001-0128-4.
[27] Mukherjee S, Ghosh AK. Flow visualization and estimation of strain and strain-rate during friction stir process. Mater Sci Eng, A 2010;527:5130–5. https://doi.org/10.1016/j.msea.2010.04.091.
[28] Masaki K, Sato YS, Kokawa H. Experimental simulation of recrystallized microstructure in friction stir welded Al alloy using a plane-strain compression test. Scripta Mater 2008;58:355–60. https://doi.org/10.1016/j.scriptamat.2007.09.056.
[29] Arora A, Zhang Z, De A, DebRoy T. Strains and strain rates during friction stir welding. Scripta Mater 2009;61:863–6. https://doi.org/10.1016/j.scriptamat.2009.07.015.
[30] Khan NZ, Bajaj D, Siddiquee AN, Khan ZA, Abidi MH, Umer U, et al. Investigation on effect of strain rate and heat generation on traverse force in FSW of dissimilar aerospace grade aluminium alloys. Metals 2019;12:1641.

[31] Buffa G, Hua J, Shivpuri R, Fratini L. Design of the friction stir welding tool using the continuum based FEM model. Mater Sci Eng, A 2006;419:381–8. https://doi.org/10.1016/j.msea.2005.09.041.
[32] Nandan R, Roy GG, Debroy T. Numerical simulation of three-dimensional heat transfer and plastic flow during friction stir welding. Metall Mater Trans A 2006;32:1247–59.
[33] Zhang Z, Wu Q. Numerical studies of tool diameter on strain rates, temperature rises and grain sizes in friction stir welding. J Mech Sci Technol 2015;29:4121–8. https://doi.org/10.1007/s12206-015-0906-3.
[34] Mcqueen HJ, Hockett JE. Microstructures of aluminum compressed at various rates and temperatures. Metall Trans 1970;1:2997–3004.
[35] Razmpoosh MH, Zarei-hanzaki A, Imandoust A. Effect of the Zener-Hollomon parameter on the microstructure evolution of dual phase TWIP steel subjected to friction stir processing. Mater Sci Eng, A 2015;638:15–9. https://doi.org/10.1016/j.msea.2015.04.022.
[36] McQueen HJ, Jonas JJ. Plastic deformation of materials. New York: Academic Press; 1975.
[37] Colligan K. Material flow behavior during friction stir welding of aluminum. Weld J 1999;78:229–37.
[38] Suhuddin UFHR, Mironov S, Sato YS, Kokawa H. Grain structure and texture evolution during friction stir welding of thin 6016 aluminum alloy sheets. Mater Sci Eng, A 2010;527:1962–9. https://doi.org/10.1016/j.msea.2009.11.029.
[39] Liu XC, Sun YF, Nagira T, Ushioda K, Fujii H. Strain rate dependent micro-texture evolution in friction stir welding of copper. Materialia 2019;6:100302. https://doi.org/10.1016/j.mtla.2019.100302.
[40] Liu XC, Sun YF, Nagira T, Ushioda K, Fujii H. Evaluation of dynamic development of grain structure during friction stir welding of pure copper using a quasi in situ method. J Mater Sci Technol 2019;35:1412–21. https://doi.org/10.1016/j.jmst.2019.01.018.
[41] Chen ZW, Pasang T, Qi Y. Shear flow and formation of nugget zone during friction stir welding of aluminium alloy 5083-O. Mater Sci Eng, A 2008;474:312–6. https://doi.org/10.1016/j.msea.2007.05.074.
[42] Xu N, Feng R, Ren Z, Gu B, Song Q, Bao Y. Improvement of microstructure and mechanical properties of AZ61 Mg alloys subjected to rapid cooling friction stir welding. Sci Technol Weld Join 2021;26:503–12. https://doi.org/10.1080/13621718.2021.1957630.
[43] Ahmad Shah LH, Sonbolestan S, Midawi RH, Walbridge S, Gerlich A. Dissimilar friction stir welding of thick plate AA5052-AA6061 aluminum alloys: effects of material positioning and tool eccentricity. Int J Adv Manuf Technol 2019;105:889–904. https://doi.org/10.1007/s00170-019-04287-9.
[44] Cordray DR, Kaplan LR, Woyciesjes PM, Kozak TF. Solid-liquid phase diagram for ethylene glycol + water. Fluid Phase Equil 1996;117:146–52.
[45] Suhuddin UFHR, Mironov S, Sato YS, Kokawa H, Lee CW. Grain structure evolution during friction-stir welding of AZ31 magnesium alloy. Acta Mater 2009;57:5406–18. https://doi.org/10.1016/j.actamat.2009.07.041.
[46] Nunes Jr AC. Metal flow in friction stir welding. Mater Sci Technol. Cincinnati, OH USA: 2006/ASM Int.; 2006. p. 15–9.
[47] Schneider J, Nunes AC. Characterization of plastic flow and resulting microtextures in a friction stir weld. Metall Mater Trans B 2004;35:777–83. https://doi.org/10.1007/s11663-004-0018-4.
[48] Kaufman JG. Aluminum alloy database. Knovel; 2004.
[49] Schneider J, Beshears R, Nunes AC. Interfacial sticking and slipping in the friction stir welding process. Mater Sci Eng, A 2006;435–436:297–304. https://doi.org/10.1016/j.msea.2006.07.082.
[50] ASTM. Standard test methods for determining average grain size. 2013.
[51] Kumar R, Pancholi V, Bharti RP. Material flow visualization and determination of strain rate during friction stir welding. J Mater Process Technol 2018;255:470–6. https://doi.org/10.1016/j.jmatprotec.2017.12.034.
[52] Yutaka SS, Hiroyuki H, Ikeda K, Enomoto M, Jogan S, Hashimoto T. Microtexture in the friction-stir weld of an aluminum alloy. Metall Mater Trans A Phys Metall Mater Sci 2001;32:941–8. https://doi.org/10.1007/s11661-001-0351-z.
[53] Field DP, Nelson TW, Hovanski Y, Jata KV. Heterogeneity of crystallographic texture in friction stir welds of aluminum. Metall Mater Trans A 2001;32:2869–77. https://doi.org/10.1007/s11661-001-1037-2.
[54] Ahmed MMZ, Wynne BP, Rainforth WM, Addison A, Martin JP, Threadgill PL. Effect of tool geometry and heat input on the hardness , grain structure, and crystallographic texture of thick-section friction stir-welded aluminium. Metall Mater Trans A 2019;50:271–84. https://doi.org/10.1007/s11661-018-4996-2.
[55] Fonda RW, Bingert JF. Texture variations in an aluminum friction stir weld. Scripta Mater 2007;57:1052–5. https://doi.org/10.1016/j.scriptamat.2007.06.068.
[56] Fonda RW, Knipling KE, Rowenhorst DJ. EBSD analysis of friction stir weld textures. JOM 2014;66:149–55. https://doi.org/10.1007/s11837-013-0802-1.
[57] Galliano S, Bella F, Piana G, Giacona G, Viscardi G, Gerbaldi C, et al. Finely tuning electrolytes and photoanodes in aqueous solar cells by experimental design. Sol Energy 2018;163:251–5. https://doi.org/10.1016/j.solener.2018.02.009.
[58] Bella F, Sacco A, Pugliese D, Laurenti M, Bianco S. Additives and salts for dye-sensitized solar cells electrolytes: what is the best choice? J Power Sources 2014;264:333–43. https://doi.org/10.1016/j.jpowsour.2014.04.088.
[59] Bella F, Pugliese D, Nair JR, Sacco A, Bianco S, Gerbaldi C, et al. A UV-crosslinked polymer electrolyte membrane for quasi-solid dye-sensitized solar cells with excellent efficiency and durability. Phys Chem Chem Phys 2013;15:3706–11. https://doi.org/10.1039/c3cp00059a.
[60] Fawzy MA, Darwish H, Alharthi S, Al-Zaban MI, Noureldeen A, Hassan SHA. Process optimization and modeling of Cd2+ biosorption onto the free and immobilized Turbinaria ornata using Box–Behnken experimental design. Sci Rep 2022;12:1–18. https://doi.org/10.1038/s41598-022-07288-z.
[61] van Sluijs B, Maas RJM, van der Linden AJ, de Greef TFA, Huck WTS. A microfluidic optimal experimental design platform for forward design of cell-free genetic networks. Nat Commun 2022;13:1–11. https://doi.org/10.1038/s41467-022-31306-3.